Title

Actin modulates shape and mechanics of tubular membranes.

Journal

Science Advances, 6(17)

Authors

Allard, A

Bouzid, M

Betz, T

et al.

Publication Date

2020-04-01

DOI

10.1126/sciadv.aaz3050

Peer reviewed

CELL BIOLOGY

Actin modulates shape and mechanics of tubular membranes

A. Allard[1,2], M. Bouzid[3], T. Betz[4], C. Simon[1], M. Abou-Ghali[1], J. Lemière[1], F. Valentino[1], J. Manzi[1], F. Brochard-Wyart[1], K. Guevorkian[1], J. Plastino[1], M. Lenz[3,5], C. Campillo[2]*, C. Sykes[1]*

The actin cytoskeleton shapes cells and also organizes internal membranous compartments. In particular, it interacts with membranes for intracellular transport of material in mammalian cells, yeast, or plant cells. Tubular membrane intermediates, pulled along microtubule tracks, are formed during this process and destabilize into vesicles. While the role of actin in tubule destabilization through scission is suggested, literature also provides examples of actin-mediated stabilization of membranous structures. To directly address this apparent contradiction, we mimic the geometry of tubular intermediates with preformed membrane tubes. The growth of an actin sleeve at the tube surface is monitored spatiotemporally. Depending on network cohesiveness, actin is able to entirely stabilize or locally maintain membrane tubes under pulling. On a single tube, thicker portions correlate with the presence of actin. These structures relax over several minutes and may provide enough time and curvature geometries for other proteins to act on tube stability.

INTRODUCTION

Membranes in cells are the boundaries of numerous internal compartments such as organelles and vesicles. These membranous structures constantly reorganize during intracellular trafficking, a process ensuring the targeted movement of substances in the cell interior. For example, flat membrane surfaces within the endoplasmic reticulum mature into highly curved cylinders and spheres (*1*). In particular, trafficking involves tubular intermediates pulled by molecular motors walking on microtubules (*2*). These dynamical rearrangements of membranes motivated the identification and the study of specialized proteins that bind to the membrane and directly act on its curvature (*3*–*5*). However, the orchestration of morphological changes needs pauses and shape stabilization processes that are often neglected (*1*).

Moreover, experiments on living cells show that the actin cytoskeleton is associated with tubular membrane intermediates. But how actin is involved in tube fate remains an open question (*6*, *7*). An attractive idea is that actin might play a role by applying physical forces and stresses, which could ultimately lead to tube scission. Alternatively, an actin layer could have a stabilizing effect on a membrane, as observed in the maintenance of cisternae in the Golgi apparatus in cells (*1*) and when actin filaments are adsorbed on a liposome membrane in vitro (*8*). These hypotheses are difficult to address in the complex intracellular environment. Furthermore, the size of transport vesicles and width of membrane tubes, between ten to hundred nanometers, are comparable with the actin network meshsize. This questions whether actin polymerization could affect tube morphology.

Here, we isolate the role of the actin cytoskeleton on membrane tube morphology in a biomimetic assay made of a membrane tube at the surface of which we polymerize an actin network. The preformed membrane tube is extruded from a liposome and held by an optically trapped bead. These tubes are stable under a nonzero point force $F = 2\pi\sqrt{2\kappa\sigma}$, where κ is the membrane bending energy and σ is the membrane tension (*9*). An adapted microinjection system sequentially delivers the activator of actin polymerization targeted to the membrane, then actin monomers that polymerize on the tube surface. The actin network is branched through the actin related proteins 2/3 (Arp2/3) complex, thus mimicking the situation in cells (*10*, *11*). We show here that, in the presence of an actin sleeve, a membrane tube can be stable even when the external pulling force vanishes. The membrane tube, surrounded by its actin sleeve, can be further pulled by the optical tweezer, at a force and a speed mimicking the pulling of membrane tubes by molecular motors walking on microtubules (*12*).

The actin network, made of entangled actin branches, produces a variety of outcomes under pulling, which depend on the thickness of the actin sleeve around the membrane tube. At a sleeve thickness higher than a few hundreds of nanometers, the network is unable to disentangle, and a sheath of actin remains around the membrane tube that maintains its radius. We show that less than 1 min of network growth is enough to obtain a stabilization of the tubular structure of the membrane that is robust and lasts for tens of minutes. At smaller sleeve thicknesses, discontinuous regions appear, and smaller tube radii are observed in portions where the actin sleeve is absent. Therefore, we never observe actin-induced scission of these membrane tubes, but rather, actin provides a way of modulating the radius of tubes along their length.

RESULTS

Actin network growth around a membrane tube

We polymerize a branched actin network at the surface of a preformed membrane tube through the activation of the Arp2/3 complex. We use a histidine-tagged version of pVCA, the proline-rich domain–verprolin homology–central–acidic sequence from human Wiskott–Aldrich syndrome protein (WASP), to activate the Arp2/3 complex (Materials and Methods). This pVCA binds to nickel lipids incorporated in the membrane and therefore activates actin

[1]Laboratoire Physico Chimie Curie, Institut Curie, PSL Research University, CNRS UMR168, Paris, France. [2]LAMBE, Université Évry Val d'Essonne, CNRS, CEA, Université Paris-Saclay, Évry, France. [3]LPTMS, CNRS, University of Paris-Sud, Universit Paris-Saclay, 91405 Orsay, France. [4]Institute of Cell Biology, Center for Molecular Biology of Inflammation, Cells in Motion Cluster of Excellence, Münster University, Von-Esmarch-Strasse 56, D-48149 Münster, Germany. [5]Laboratoire de Physique et Mécanique des Milieux Hétérogènes, UMR 7636, CNRS, ESPCI Paris, PSL Research University, Université Paris Diderot, Sorbonne Université, Paris 75005, France.
*Corresponding author. Email: clement.campillo@univ-evry.fr (C.C.); cecile.sykes@curie.fr (C.Sy.)

polymerization at the tube surface. This experimental system allows us to isolate the pure mechanical role of actin on membrane deformation and maintenance, independently of any proteins that are known to link lipids to actin polymerization activators in a more physiological context. Whereas additional proteins may impose an initial curvature to the membrane and ease the deformation process, we recently showed that membrane deformations mimicking endocytosis and filopodia formation can be achieved exclusively by actin dynamics (*13*). In our experimental system and to avoid unnecessary actin polymerization in the solution, we provide actin monomers only once the membrane is activated for polymerization. The time at which actin polymerization starts on the membrane tube is rigorously controlled by proceeding sequentially as follows. First, the preformed fluorescent membrane tube, maintained by an optically trapped bead, is bathed in a solution containing the other necessary proteins [P-solution with the Arp2/3 complex, profilin, and capping protein (CP); Materials and Methods and Fig. 1A, a]. Second, pVCA is targeted to the membrane by microinjection close to the tube; proper injection is monitored by a sulforhodamine dye (Fig. 1A, b). Third, actin monomers are microinjected, and this moment sets the time (t_i in Fig. 1A, c) at which actin polymerization starts around the tube. Actin becomes visible by fluorescence on the membrane after a few seconds (Fig. 1A, c) and continues to grow (fig. S1A). We could expect the presence of a radial stress exerted by the growing actin network in cylindrical geometry, which was observed and demonstrated in spherical geometry (*14*, *15*). However, during actin polymerization and after, we observe no detectable decrease in tube lipid intensity under the sleeve, and therefore, no decrease in tube radius. After 2 min, a sleeve of actin is obtained around the membrane tube (Fig. 1A, d), whereas it fails to form when pVCA is omitted (fig. S1, compare B and C). We define this composite system of membrane tube sheathed with an actin sleeve as "membrane-and-actin-sleeve" (MaAS).

MaAS characteristics under pulling forces comparable to the cellular situation

To mimic tubular intermediates pulled by molecular motors walking on microtubules, we subject MaAS to elongation by moving the stage at a controlled speed of 0.5 to 4 μm/s to reach tube lengths of 15 to 30 μm. We observe two cases. The first is an escape of the bead from the optical trap after a short MaAS elongation of less than 1 μm. In this case, the MaAS, thereafter called "escaped MaAS," retains its shape, indicating that the rigidity of the actin sleeve is strong enough to hold the bead in position even outside the trap (Fig. 1B). The tube does not retract, and this lasts for tens of minutes (fig. S2A). What we observe notably differs from a membrane tube in the absence of actin that would totally retract and reincorporate in the liposome within hundreds of milliseconds (*16*). In the second case, a MaAS continuously elongates during stage displacement and is thereafter called "elongated MaAS" once the stage is stopped (Fig. 1C). Note that the actin sleeve in elongated MaAS might be discontinuous. We then explore whether the amount of actin in the sleeve may be different in these two cases.

Actin thickness imposes MaAS fate

We visualize lipids and actin by confocal microscopy and concomitantly record the force F in the limit of 50 pN on the optically trapped bead (Materials and Methods). First, we quantify the amount of actin by measuring the total actin fluorescence intensity of MaAS before pulling, normalized by the membrane tube fluorescence (Materials and Methods). The actin content is clearly higher in escaped MaAS than in elongated MaAS (Fig. 2A). Second, force-elongation curves of escaped MaAS reveal a linear dependence of the force F as a function of the tube elongation $\Delta\ell$ (filled circles, Fig. 2B; Materials and Methods). Escaped MaAS therefore appear linearly elastic ($F = k\Delta\ell$), with an average spring constant $k = 31 \pm 6$ pN/μm. A linear force-extension curve is also observed for elongated MaAS and naked tubes with markedly lower slopes, respectively 0.38 ± 0.11 and 0.30 ± 0.09 pN/μm (Fig. 2B).

Escaped MaAS are robust elastic structures where the membrane tube remains under the sleeve. The membrane tube is held by the bead that is 3.05 μm in diameter, much larger than the membrane tube diameter. Therefore, full tube retraction is retained by the bead and the presence of the actin sleeve. In these conditions, escaped MaAS behavior is dominated by the contribution of the actin network that elongates concomitantly with the membrane tube (fig. S2, B and C). The connection between the bead and the sleeve may occur through a strong connection to the membrane patch on the bead or through a nonspecific interaction between the actin and the bead. This is unlikely that membrane-sleeve friction could be responsible for this connection (see section S3). With this, the thickness of the actin sleeve can be estimated from the elastic spring constant k. The actin network elastic modulus E was measured previously in similar experimental conditions as 10^3 to 10^4 Pa (*17*). The spring constant k of the actin sleeve is related to the sleeve cross-sectional area S, MaAS length L, and E as $k = ES/L$. With $L = 15$ to 30 μm and our experimental measurement of $k \simeq 31$ pN/μm, we find $S = 0.05$ to 0.9 μm^2 that leads to a sleeve radius of $e = \sqrt{S/\pi} \simeq 120$ to 550 nm. Note that we neglect here the hollowness of the sleeve, which has a contribution to the section area that is one order of magnitude lower for a typical radius of 25 nm in our experiments.

Simulation of a branched actin network under deformation

To account for the difference in MaAS fate depending on the actin content of the actin sleeve (Fig. 2A), we perform detailed molecular dynamics simulation of an entangled branched actin network under deformation [Supplementary Materials and (*18*–*23*)]. Physically, our experimental observations suggest that thin actin sleeves are less cohesive than their thicker counterparts and, thus, tend to fall apart to yield an elongated MaAS. Conversely, we reason that actin filaments in thicker sleeves are more extensively entangled, implying a more robust structure resulting in an escaped MaAS. To validate this picture and determine the minimal actin thickness required for an escaped MaAS, we apply a uniaxial quasi-static deformation along the x axis of simulated networks with different thicknesses (Fig. 2C). While internal local stresses remain low in thin networks, large and strongly heterogeneous stresses develop in thick networks, since entangled filaments pull on one another to maintain network cohesion (Fig. 2C, compare bottom to top). Assuming an actin persistence length of 10 μm (*24*, *25*) and a network meshsize inferred from simulations, $\ell_{mesh} = 30$ nm (*26*) in the same protein mix as here, we derive the corresponding force-extension curves for a whole cylindrical actin sleeve of inner radius 25 nm and variable thickness ℓ_z, which is shown in Fig. 2D. While all networks display an initial linear response, in thin networks, the force peaks at a relatively modest value F_{tear}, following which the network looses its cohesion and the force decreases. By contrast, thick networks display much larger tearing forces F_{tear}. Figure 2E compares this tearing force to our maximum tweezing force of 50 pN (dashed line) for different values of network

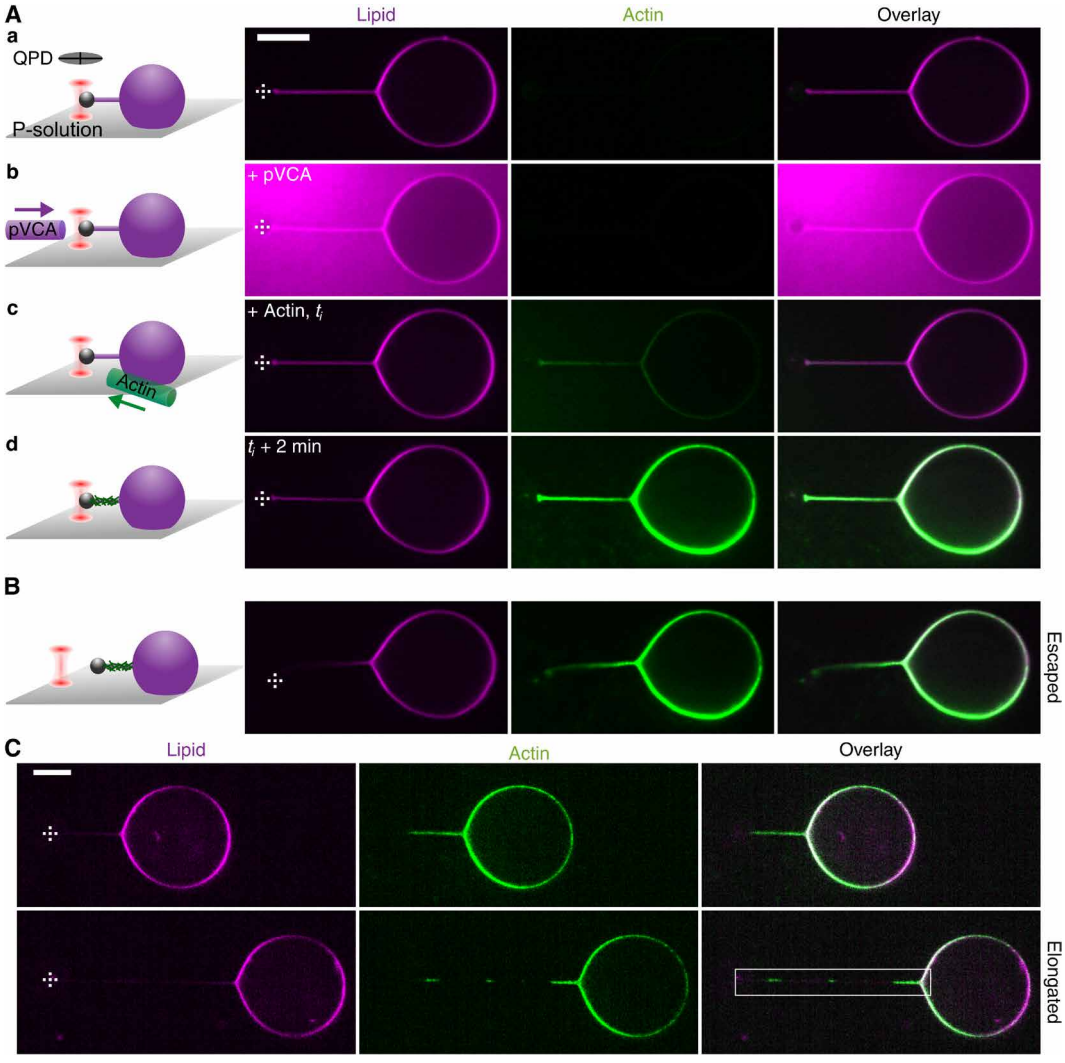

Fig. 1. Effect of an actin sleeve on membrane tube stability. Lipids (magenta) and actin (green) are observed by spinning disk confocal imaging. (**A** and **B**) Left column: Scheme of each step toward MaAS formation. (A) (a) Preformed tube held by optical tweezer, (b) microinjection of pVCA in a sulforhodamine-B solution, (c) microinjection of monomeric actin at t_i, and (d) the membrane tube is sheathed with an actin sleeve within 2 min. A quadrant photodiode (QPD) images the laser beam. (B) Escaped MaAS and (**C**) elongated MaAS before (top) and after (bottom) pulling; the white box indicates the location of the elongated MaAS. Scale bars, 10 μm. Dashed crosses indicate bead center.

thicknesses ℓ_z. For any sleeves whose tearing force exceeds the maximum tweezing force, the optical tweezer will give in before the sleeve does, and based on Fig. 2E, we thus predict that any sleeve thicker than ~10 meshes results in an escaped MaAS, while a thinner sleeve yields an elongated MaAS. This corresponds to a critical sleeve radius of $e \sim 300$ nm, consistent with our experimental estimate above.

This phase diagram reveals that the rigidity of the actin network increases almost exponentially as a function of the number of meshes. Our findings highlight that a small variation of the amount of actin, through a difference in a few units of meshes, displaces the system efficiently from a stable to an unstable state.

Morphology of elongated MaAS

A notable observation in elongated MaAS is that the membrane tube is continuously present, whereas the actin sleeve appears discontinuous (Fig. 3A). Higher actin fluorescence along the tube correlates with higher lipid fluorescence, revealing that a thicker membrane tube is present under stable actin sleeve regions (Fig. 3A). To quantify this effect, for each MaAS, we define the membrane tube radius r_M where the actin signal is maximal, and r_m where the actin signal is minimal (including equal to zero) along the tube (respectively "M" and "m" in Fig. 3A and fig. S3, A to C). With r_0 the membrane tube radius before the MaAS is pulled, the relative variation of radius reads $\delta r/r_0 = (r_M - r_m)/r_0$ and is obtained directly from lipid fluorescence intensities (Fig. 3A; fig. S3, A to C; and Materials and Methods). Moreover, elongating a MaAS reveals three different situations that are sketched in Fig. 3B: In two of them, the sleeve maintains roughly its initial length but sits either next to the bead (Fig. 3, A and B, *a*) or next to the liposome (Fig. 3B, *b*), and in the third situation, the actin sleeve extends together with the membrane tube (Fig. 3B, *c*). The heterogeneity along the tube, through the ratio $\delta r/r_0$, is close to zero before pulling ("Ref" condition; Fig. 3B) and increases when the MaAS is elongated, revealing the presence of radius heterogeneity along the tube (*a*, *b*, and *c*; Fig. 3B). According to our classification, this increase is

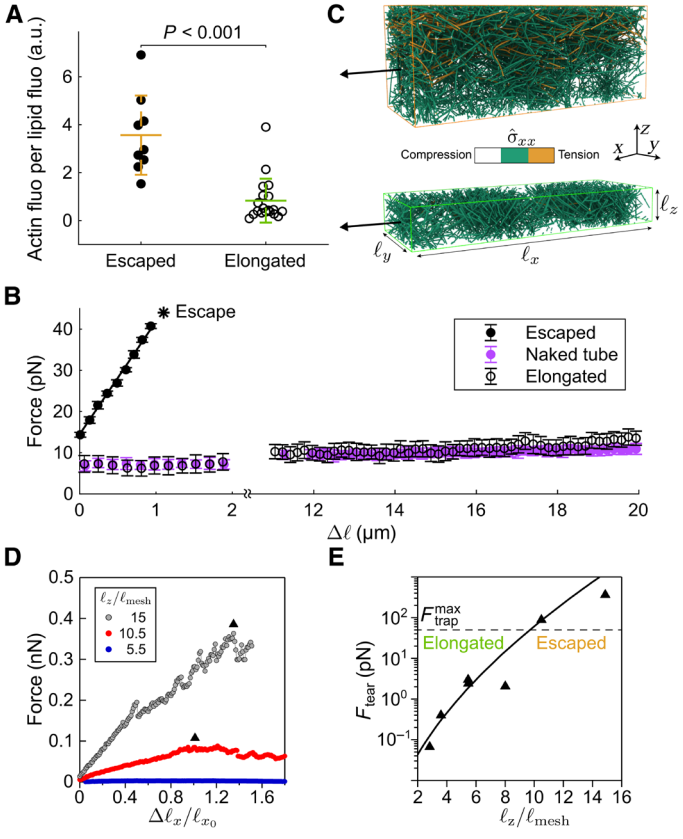

Fig. 2. Actin sleeve thickness drives MaAS fate. (**A** and **B**) Escaped (filled circles; $n = 8$) and elongated (opened circles; $n = 17$) MaAS. Data are shown as means ± SD. (A) Quantification of actin fluorescence per lipid fluorescence depending on MaAS fate. *P* values are calculated using the *t* test. a.u., arbitrary unit. (B) Force-elongation curves for MaAS and a naked tube (light magenta filled circles; $n = 15$). The star symbol indicates the length at which the MaAS escapes. (**C**) Snapshots of two branched actin network networks for different thicknesses ℓ_z (top $\ell_z = 10.5\ell_{mesh}$; bottom $\ell_z = 5.5\ell_{mesh}$) under uniaxial deformation along the *x* axis. The two configurations correspond to a deformation of ~150%. Colors indicate the local longitudinal stress $\hat{\sigma}_{xx}$ at the scale of a monomer, ranging from yellow for tension to white for compression. (**D**) Average force *F* extrapolated for a cylindrical sleeve with inner radius $R_0 = 25$ nm and variable thickness ℓ_z, implying an outer radius $R_0 + \ell_z$ as a function of the deformation $\Delta\ell_x/\ell_{x0} = (\ell_x - \ell_{x0})/\ell_{x0}$, with ℓ_{x0} the initial size, for different network thicknesses. Triangles indicate the maximum force F_{tear} that the network can bear before falling apart. (**E**) Phase diagram representing F_{tear} as a function of the gel thickness. The dashed black line shows the optically trapped bead force limit of about 50 pN. Actin sleeves larger than ~10 meshsizes should, thus, display an escaped MaAS behavior.

significant for the *b*-type, where the actin sheath stays close to the liposome. Independently of the (*a*, *b*, and *c*) classification, the relative variation of radius increases in a high actin content situation (Fig. 3C).

Theoretical consideration of MaAS elongation

The increase in force necessary to obtain an elongated MaAS is proportional to its elongation (Fig. 2B), and the proportionality factor is slightly higher for *b*-types (fig. S4A). This may be due to a hindrance of lipid flow under the actin sleeve that is higher in *b*-types than in *a*- and *c*-types. To account for this observation, we propose a model of force buildup assuming that lipids reaching the bare part of the tube are forced to go through the actin sleeve. As sketched in the inset in Fig. 3D, we model the bare section of the membrane tube as a cylinder of a length ℓ and radius r_m, which both vary over the course of the tube extension, and the actin sleeve section has a fixed length L and a radius r_M, which may also vary. The sleeve and the liposome are sheathed by actin, which binds to the membrane with an energy per area $W > 0$. W accounts for the resistance from the actin sheath to membrane thinning. This yields the following modified Helfrich energy function for the system (*27*)

$$H = 2\pi\ell\, r_m\left(\frac{\kappa}{2\,r_m^2} + \sigma + W\right) + 2\pi L r_M\left(\frac{\kappa}{2\,r_M^2} + \sigma\right) \qquad (1)$$

where κ is the bending rigidity of the membrane, and σ is the tension of the liposome.

Initially, the bead is in close contact with the actin sleeve, implying that $\ell = 0$, from which we deduce $r_{M,initial} = r_0 = \sqrt{\kappa/2\sigma}$ from the minimization of H. We assume that the tube is pulled fast enough to prevent any substantial flow of lipids from the liposome to the MaAS. In these conditions, ℓ increases under the constraint of constant area $A = 2\pi r_m\ell + 2\pi r_M L$. This assumption is confirmed by the conservation of the tube surface during pulling for *b*-type MaAS (constant integrated fluorescence along the tube; fig. S4B). We, thus, minimize H with respect to r_m and r_M while fixing A for a given ℓ (Supplementary Materials). The resulting tube force reads $F = dH/d\ell$. For small values of W/σ, we thus obtain

$$F = \frac{2\pi\kappa}{r_0}(1 + \ell/L) \qquad (2)$$

Therefore, F increases linearly with ℓ, in agreement with the observations of Fig. 2B upon tube pulling (Supplemental Materials). Equation 2 implies an apparent spring constant $k = dF/d\ell = 2\pi\kappa/(r_0 L)$, and fitting this relation with our experimental measurements leads to $\kappa = 17\ k_BT$ (Fig. 3D) close to the bare membrane value of 12 k_BT, where k_BT is the thermal energy. We, thus, validate our assumption of lipid flow hindrance under the actin sleeve.

For the *a*- and *c*-type configurations of Fig. 3B and fig. S4A, the slope of the initial force elongation is lower and close to the one of naked tubes, consistent with our assumption that the contact between the sleeve and the tube is largely responsible for limiting the lipid flow to the MaAS.

This theoretical description allows us to estimate the difference in radii between the actin sleeve and bare tube sections, through a calculation to next order in W/σ, yielding

$$\frac{r_M - r_m}{r_0} = \frac{W}{2\sigma}\frac{1}{(1 + \ell/L)^3} \qquad (3)$$

In practice, this expression gives a good qualitative description of the ℓ dependence of the radius difference even for fairly large values of $W/\sigma \simeq 1$ (Supplementary Materials). While comparing these predictions with our experimental measurements would, in principle, allow a determination of the actin binding energy to the membrane, we find in practice that these measurements do not yield a consistent value for W/σ, probably in part because the tension σ of the vesicle is not controlled in our experiment (Supplementary Materials). As a result, rather than determining the specific value of W/σ, in the following, we place ourselves in the small W/σ regime, which yields results qualitatively similar to the ones obtained at larger W/σ (fig. S5).

Relaxation of elongated MaAS

When maintained for several minutes, we observe that lipid fluorescence homogenizes along the tube as a function of time in elongated

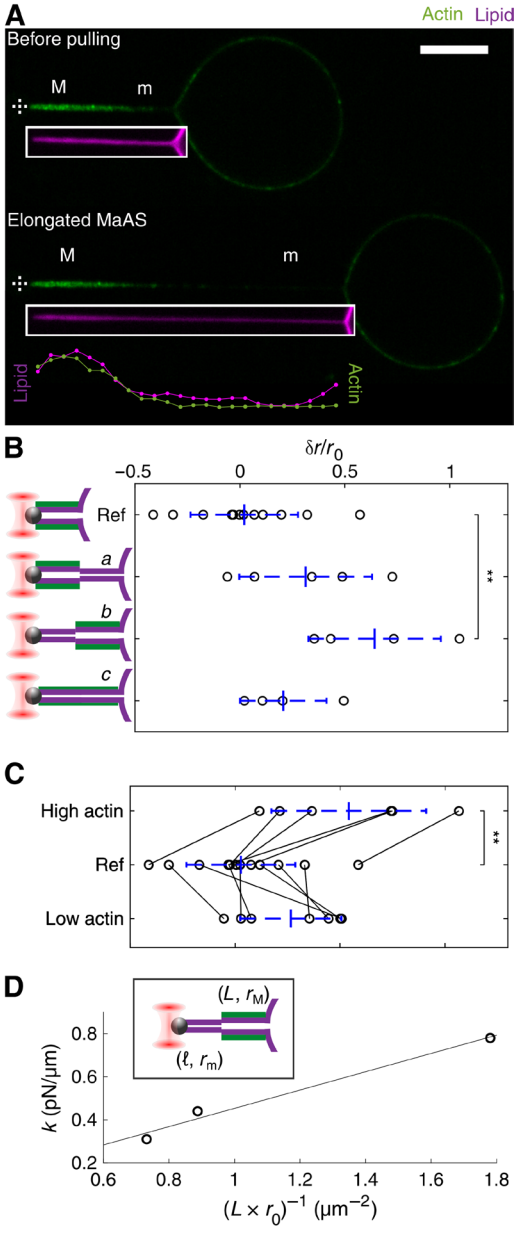

Fig. 3. Membrane tube radius in elongated MaAS. (**A**) Representative confocal images before pulling for reference (top) and after elongation (bottom). Magenta and green correspond respectively to lipid and actin. The lipid image is displaced in the white rectangle right below the actin image for clarity. M and m regions are respectively defined as maximal and minimal actin intensity regions of the elongated MaAS (bottom) or before pulling (top). Graphs represent lipid and actin intensities along the elongated MaAS. Scale bar, 10 μm. Dashed crosses indicate bead center. (**B** and **C**) Relative difference in membrane tube radius between M and m regions defined in (A). (B) Values corresponding to classification schemed on the left (*a*, *b*, and *c*). (C) "High actin" and "Low actin" refer respectively to actin content of elongated MaAS above and below average in Fig. 2A; reference condition (Ref) is before pulling. Lines connect same MaAS before and after elongation. (**D**) Proportionality factor of force-elongation curve, for *b*-type MaAS, as a function of $(L \times r_0)^{-1}$. In the inset, parameters used for theoretical description of *b*-type MaAS. Data are shown as means ± SD in (B) and (C). *P* values calculated using *t* test. $^{**}P < 0.01$.

MaAS (dotted lines; Fig. 4, A and B), more visible in case *b* (Fig. 4B), where the heterogeneities are higher. Simultaneously, the force relaxes and mirrors radius relaxation (Fig. 4, C and D). The characteristic time of force relaxation, estimated through an exponential fit, is longer for elongated MaAS than for naked tubes (Fig. 4E).

During the initial rapid pulling step, the membrane becomes tenser and thinner than would be the case for a pure membrane tube. This results in the force increase of Eq. 2 for *b*-type. As the bead is held in position, relaxation occurs through lipids slowly flowing from the liposome toward the MaAS. The decrease in lipid mobility in a membrane tube in the presence of an actin sleeve is confirmed by fluorescence recovery after photobleaching (FRAP) experiments [fig. S6, Supplementary Materials, and (*28*)]. By balancing the membrane forces driving this flow with the dissipation due to the friction of a membrane of viscosity η against a density ρ of actin attachment points, we compute the force relaxation dynamics to lowest order in W/σ as

$$F = \frac{2\pi\kappa}{r_0}\left[1 - \frac{\ell(2L+\ell)}{(L+\ell)^2}e^{-t/\tau}\right]^{-1/2} \quad (4)$$

where the relaxation time is given by (Supplementary Materials)

$$\tau = \frac{\rho\eta L(L+\ell)\,r_0^2}{\kappa} \quad (5)$$

The fit of our data using Eqs. 4 and 5 leads us to derive $\rho\eta = (3 \pm 1) \times 10^6$ Pa · s/m ($n = 4$ *b*-types). By assuming we saturate all the binders, we can estimate in our experiment $\rho = 10^{15}$ m^{-2} (*29*, *30*), which leads to $\eta = 3 \pm 1 \times 10^{-9}$ Pa · s · m close to previously published estimate $\eta = 10^{-8}$ Pa · s · m (*31*, *32*).

Therefore, elongated MaAS relaxation can be explained by the friction of lipids under the actin sleeve for *b* cases. For cases *c*, the friction is lower, and therefore, the relaxation time is much smaller and close to the one of naked tubes.

Elongated MaAS retraction

When the trap is turned off, we observe either partial or complete retraction (Fig. 5). Partial retraction ends up with the presence of an actin sleeve in between the bead and the liposome, and its characteristic retraction time is 1.3 ± 0.3 s ($n = 10$; Fig. 5A and open circles in Fig. 5, C and D). Total retraction ends up with the bead at the liposome surface within a time that is smaller than 0.39 ± 0.10 s ($n = 7$; crosses in Fig. 5, C and D), similar to when pVCA is omitted (Fig. 5B and gray filled circles in Fig. 5C). Regions of membrane tubes devoid of actin in elongated MaAS noticeably thicken when the MaAS retracts, whereas they remain intact under the sleeve (arrowheads; Fig. 5A). Note that such a situation of a MaAS at zero force provides an even larger range of tube radii than when the tube is under force.

Actin network in all MaAS types

All three MaAS types presented above are gathered in a diagram with their corresponding actin and lipid fluorescence intensities and reveal distinct regions depending on their types (see sectors or bands respectively in Fig. 5E or inset). We find that for a given tube radius, the amount of actin determines MaAS fate: Escaped MaAS occurs at the highest actin content that corresponds to highly entangled networks [Figs. 5E (filled circles) and 2C (top)], and elongated MaAS separate in two sectors depending on their retraction fate (emptied circles and crosses in Fig. 5E). Note that thin tubes (lipid intensity low) cannot provide any sufficient support for the growth of an actin sleeve (empty

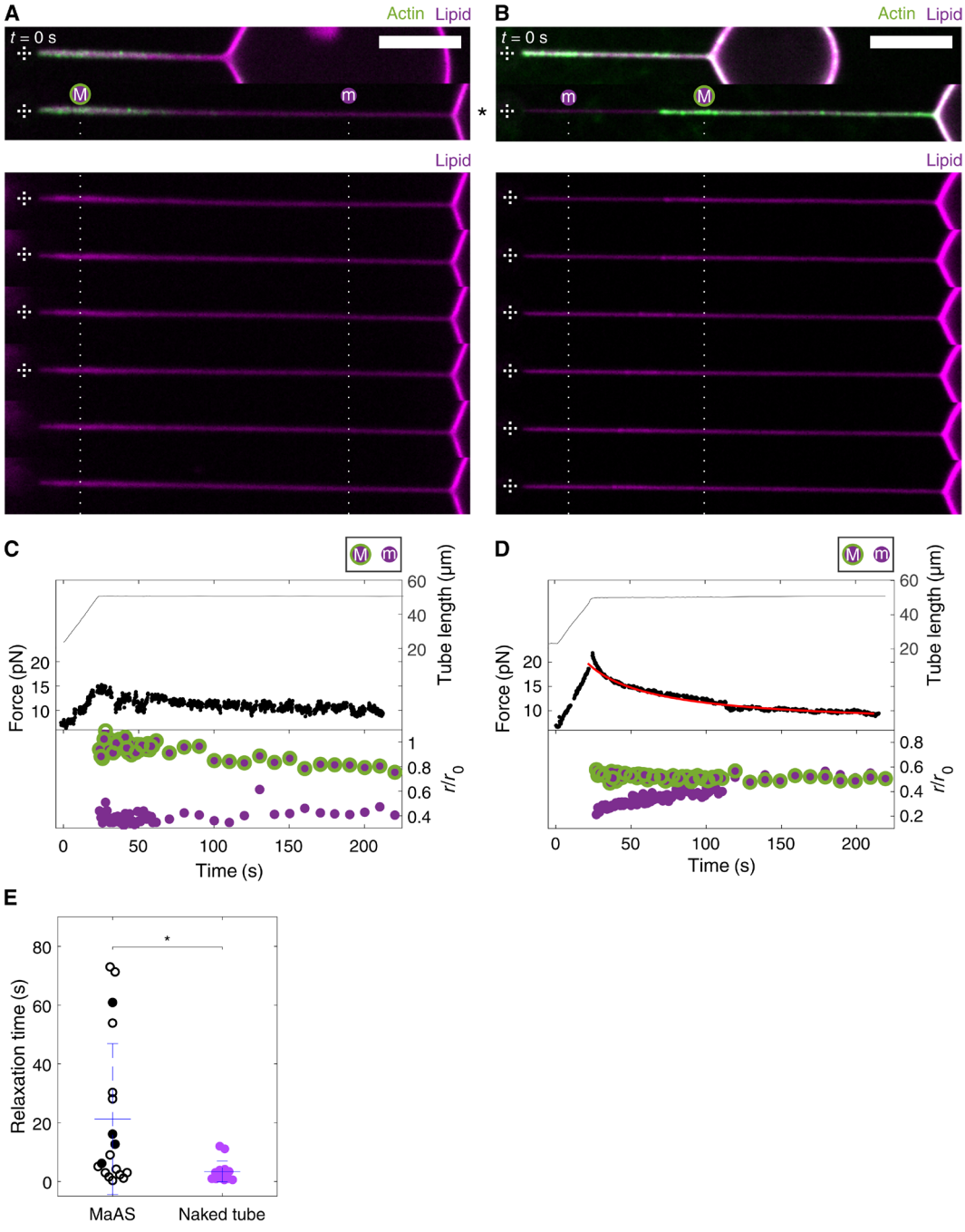

Fig. 4. Elongated MaAS relaxation. (**A** and **B**) Representative confocal images of relaxing elongated MaAS (images every 30 s). Scale bars, 10 µm. Dashed crosses indicate bead center. Dotted lines follow lipid fluorescence relaxation. (**C** and **D**) Corresponding curves as a function of time for length, force, and relative membrane tube radii associated with m and M regions defined in Fig. 3A and Materials and Methods. Time 0 corresponds to the start of MaAS pulling. In red, the fitting curve from Eq. 4 using experimental values $\ell = 26.5$ µm and $L = 22.1$ µm. (**E**) Relaxation time of the force for elongated MaAS and naked tubes, using an exponential decay (Materials and Methods). Black filled circles point *b*-type MaAS. *P* values calculated using *t* test. *$P < 0.05$.

sector zone top left corner; Fig. 5E), as their radius are too small to authorize correct building and growth of the actin network. Considering that we saturate nickel lipid sites with pVCA, the concentration of activators of polymerization at the surface of tubes is equal to the concentration of nickel lipids and therefore proportional to the lipid intensity I_{lipid}. Besides, we assume that the quantity of actin I_{actin} in the sleeve is proportional to the quantity of activators. Hence, the ratio I_{actin}/I_{lipid} depends on the sleeve thickness and varies between sectors in Fig. 5E (or bands in inset), depending on the nature of MaAS (escaped, elongated, partial, or total retraction).

We take our estimates above for the sleeve radius in escaped MaAS (10 meshsizes; Fig. 2B) and matching it to the escaped MaAS sector

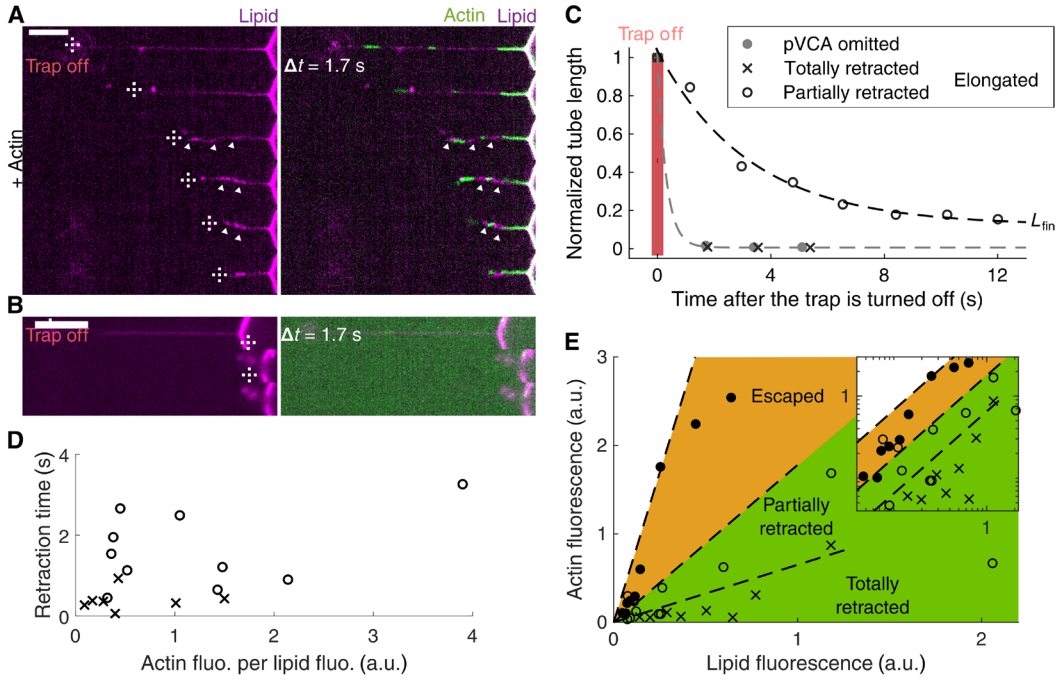

Fig. 5. Elongated MaAS retraction. (**A** and **B**) Time lapse overlay images after the trap is turned off for an elongated MaAS (A) and control (pVCA microinjection is omitted) (B). Arrowheads indicate regions devoid of actin that get thicker during retraction. Scale bars, 10 μm. Dashed crosses indicate bead center. (**C** to **E**) Empty circle, partially retracted; crosses, totally retracted. (C) Tube length as a function of time after the trap is turned off for elongated MaAS or when pVCA is omitted (gray filled circles). (D) Retraction time as a function of actin content. (E) Actin fluorescence as a function of lipid fluorescence. Full circles are escaped MaAS. Dotted lines separate sectors. We use the orthogonal residue method, where we minimize the orthogonal distance between data and the linear regression to approximate sector separations. Elongated MaAS are in the green region, and escaped MaAS are in the orange region. Totally and partially retracted MaAS are separated in sectors inside the green region. Inset: Log-log representation, previous triangular sections then become bands here.

(Fig. 5E). Then, we infer sleeve radius for elongated MaAS from the slopes of the lines delimiting the corresponding sectors. We find that elongated MaAS partially retracted display a sleeve of thickness in the 45- to 120-nm range (two to four meshsizes) and that totally retracted elongated MaAS display actin sleeves of less than 45 nm (~2 meshsizes).

This experimental diagram summarizes that a sleeve thickness, estimated to 10 meshsizes (inferred from simulation data) (*26*), is enough to stabilize membrane tubes, whereas 2 to 10 meshsizes only partially stabilize them. MaAS behave like naked tubes below two meshsizes. Therefore, stabilization of membrane tubes is highly sensitive to the number of meshes. Experiments, concomitantly with previous simulations (*26*), highlight the importance of the cohesion of the actin network around a membrane tube.

DISCUSSION

In summary, MaAS diversity can be explained by the thickness of their actin sleeve. Either they are totally cohesive by filament entanglement and their behavior is controlled by the actin network elasticity, or they are extensible because actin filaments disentangle massively.

The role of actin in the morphology of intracellular membranes during trafficking or shaping the endoplasmic reticulum has been questioned in the last decade (*1*, *4*). The impressive ability of actin dynamics to change rapidly the shape of membranes (*13*, *33*–*36*) naturally points to a similar role in membrane reorganization during trafficking. However, we show here unambiguously that a branched actin network grown through the Arp2/3 complex activated at the membrane surface has a stabilizing effect on the shape of the membrane tube rather than works as a scissionner. This stabilizing mechanism is highly sensitive to a small variation in the amount of actin that builds the sleeve network.

When tubes surrounded by an actin sleeve are submitted to a pulling force, mimicking what happens during intracellular trafficking, the actin sleeve fragments, providing the formation of sections of different radii along a single tube. Thereby, some portions of membrane tubes get thinner under force, whereas they get thicker when the force vanishes. Such a mechanism allows a membrane tube to provide portions of different radii along its length. The morphology of membrane tubes and their stability are therefore fine-tuned by actin. This could explain the localization of specialized proteins such as BAR (Bin/Amphiphysin/Rvs) domain proteins that detect curvature for scission (*37*) or dynamin that actively squeezes tubes in a curvature-dependent fashion (*38*). Moreover, portions of membrane tubes of different radii are connected by neck structures that may further serve for mechanisms of membrane reorganization.

Whereas the actin network meshsize is very close to the radius of tubular intermediates in trafficking and membrane tubes in our experiments, the number of meshes, above two, is what counts to obtain a membrane tube with a variety of radii. Note that a totally stabilizing network of 10 meshes is formed in a few seconds, consistent with the characteristic time of tubular intermediate morphology changes in cells (*7*). An additional role of actin, demonstrated here for membrane tubes, is that it hinders lipid mobility, a mechanism proposed earlier to promote tube scission (*39*).

MATERIALS AND METHODS

Buffer solutions

Chemicals were purchased from Sigma-Aldrich unless specified otherwise. The internal buffer (TPI) consisted of 2 mM tris and 200 mM sucrose. The external buffer (TPE), where the polymerization occurred, contained 1 mM tris, 50 mM KCl, 2 mM $MgCl_2$, 0.1 mM dithiothreitol (DTT), 2 mM adenosine 5′-triphosphate (ATP), β-casein (0.02 g/liter), and 95 mM sucrose. TPE_{inj}, limiting actin polymerization inside the micropipette, consisted of 1 mM tris, 1 mM $MgCl_2$, 0.1 mM DTT, β-casein (0.02 g/liter), and 195 mM sucrose. TPA, a high-osmolarity buffer, contained 1 mM tris, 1 mM $MgCl_2$, 0.1 mM DTT, β-casein (0.02 g/liter), and 395 mM sucrose. All buffers were adjusted at pH 7.4, and their osmolarity was set at 200 mosmol/kg (400 mosmol/kg for TPA). Osmolarities were measured with a vapor pressure osmometer (Vapro 5600, Wescor, USA). G-buffer, to obtain monomeric actin, was composed of 2 mM tris, 0.2 mM $CaCl_2$, 0.2 mM DTT, and 0.2 mM ATP (pH 8.0).

Preparation of liposomes

Lipids stocks EPC (L-α-phosphatidylcholine from egg yolk), DS-PE-PEG(2000)-biotin (1,2-distearoyl-sn-glycero-3-phosphoethanolamine-*N* [biotinyl-(polyethylene glycol) 200]), and 18:1 DGS-NTA(Ni) (1,2-dioleoyl-sn-glycero-3-[(*N*-(5-amino-1-car-boxypentyl) iminodiacetic acid)succinyl]) were purchased from Avanti Polar Lipids (Alabaster, USA). Texas Red DHPE (1,2-dihexadecanoyl-sn-glycero-3-phosphoethanolamine, triethylammonium salt) was obtained from Thermo Fisher Scientific (Waltham, USA). All stocks were aliquoted in chloroform/methanol at volume ratio 5/3.

Liposomes were formed using the standard electroformation method (*40*). The lipid mix (molar ratio EPC/DGS-Ni/DSPE-PEG-biotin/Texas Red DHPE of 89.4/10/0.1/0.5) was dissolved at 2.5 g/liter in chloroform/methanol at volume ratio 5/3. A volume of 5 μl of this solution was spread on an indium tin oxide (ITO)–coated glass slide (63691610PAK; Sigma-Aldrich, Germany). The film of lipids was dried in vacuum for 2 hours. Then, the films of lipid were hydrated with TPI by assembling the two conductive slides facing each other into a chamber sealed with Vitrex (Vitrex Medical A/S, Denmark). An oscillating electric field (10 Hz, 3 V peak to peak) was applied across the chamber during 2 hours. Liposomes were stored at 4°C for up to 2 weeks.

Proteins and reagents

α-Actin purified from rabbit skeletal muscle and porcine Arp2/3 complex were purchased from Cytoskeleton (Denver, USA). Fluorescent Alexa Fluor 488 actin conjugate (actin-488) was purchased from Molecular Probes (Eugene, USA). Mouse α1β2 CP was purified as described elsewhere (*41*). His-pVCA-GST (pVCA; starting at amino acid Gln^{150}) was purified as for PRD-VCA-WAVE (*42*). Recombinant untagged human profilin produced in bacteria was purified as in (*34*). A solution of 30 μM monomeric actin containing 15% of labeled actin-488 was obtained by incubating the actin solution in G-buffer over 2 days at 4°C. Commercial proteins were used with no further purification, and all concentrations were checked by a Bradford assay.

Optical tweezer, image acquisition, and tube pulling

As previously described (*43*), we used a system that allowed us to simultaneously measure forces with the optical tweezer and record images with a spinning disk confocal microscope (CSU-X1 Yokogawa; Andor Technology, Ireland) and by a high-resolution sCMOS (scientific complementary metal-oxide semiconductor) camera (Andor Neo, Ireland). The optical tweezer were based on an infrared laser (λ = 1064 nm, *P* = 5 W; YLM-5-LP-SC, IPG Laser, Germany) controlled by an XY acousto-optic deflector (AOD) pair (MT80-A1 51,064 nm; AA Opto Electronic, France). A water immersion objective (PLAN APO VC 60× A/1.2WI IFN 25 DIC N2; Nikon, Japan) was used for imagery.

To pull a membrane tube, a streptavidin-coated polystyrene bead (3.05-μm diameter, streptavidin coated; Spherotech, Illinois, USA), which served as a handle to maintain the tube, was first trapped optically. A biotinylated liposome, slightly adherent to the bottom surface of the chamber, was then attached to the bead. By moving away the stage at a constant speed, a tube formed between the liposome and the bead. The position of the bead relative to the trap center was recorded on the basis of the back focal plane technique (*44*). We recorded the interference signal between the unscattered laser light and the light scattered by the bead, imaged on a quadrant photodiode (QPD; PDQ-30-C, Thorlabs, Germany) placed on the optical path. After proper calibration, the voltage from the QPD was proportional to the bead displacement. Trap stiffness k_{trap} was deduced from the power spectrum of the bead fluctuations around the center of the trap. We find k_{trap} = 58.4 ± 2.3 pN/μm over 25 independent experiments. Together, calibrations of the QPD and the trap stiffness provided force measurements from the bead displacement in the trap.

Last, the chamber was mounted on a two-dimensional piezo stage (MS-2000; ASI, USA) that controls its positioning and allows its displacement at a controlled velocity. The tube elongation $\Delta\ell$ was experimentally calculated from the known speed v of the stage and the position x of the bead with respect to the trap center. Then, during elongation, $vt = \Delta\ell + \Delta x$, where $\Delta x = \Delta F_{QPD}/k_{trap}$ is the relative bead displacement in the trap. Last, tube elongation yielded $\Delta\ell = vt - \Delta F_{QPD}/k_{trap}$.

Chamber and micropipette preparation

Before experiments, we sonicated glass coverslips (0.13 to 0.16 mm; Menzel Gläze, Australia) in 2-propanol for 5 min, extensively rinsed with water, and dried under filtrated compressed air. Then, the glass surface was activated by a plasma cleaner (PDC-32G; Harrick Plasma, USA) during 2 min, followed by a 30-min passivation using PLL(20)-g[3.5]-PEG(2) (0.1 g/liter; SuSos, Switzerland) in a 10 mM Hepes solution (pH 7.4). The experimental chamber was made of two glass coverslips separated by a 1-mm steel spacer. The chamber was filled with a 100-μl polymerization mix (P solution) in TPE containing 3 μM profilin, 37 nM Arp2/3 complex, 25 nM CP, 2 μl of liposomes in TPI, and 1 μl of polystyrene beads diluted 100 times in TPE.

Micropipettes were prepared from borosilicate capillaries [0.7 mm/1.0 mm for inner/outer diameter (ID/OD); Harvard Apparatus, USA], using a puller (P2000, Sutter Instrument, USA) with parameters previously described in (*43*). Micropipette tips were then microforged (MF-830, Narishige, Japan) to an internal diameter of 10 μm. Micropipettes were filled by aspirating 1 μl of the desired solution. Mineral oil was filled on the other side of the micropipette using a MicroFil (250 μm; ID, 350 μm; OD, 97 mm long; World Precision Instruments, UK). We prepared two micropipettes: the first one contained 2 μM pVCA, sulforhodamine-B (0.01 g/liter; to monitor the microinjection), in TPE; and the second one contained 3 μM actin-488 and 3 μM profilin, in TPEinj, adjusted to the osmolarity of 200 mosmol/kg with TPA.

Note that profilin was present in the actin microinjection pipette and in the P solution, so that actin polymerization was prevented in the micropipette and in solution and occurred only at the membrane surface. Each micropipette was set up into the chamber, one on each

side connected to two separated reservoirs to control the injection pressure. The chamber was sealed on each side by adding mineral oil to block evaporation over the time of the experiment.

Fluorescence intensity

We defined a box centered around the tube, the height of which was kept at 50 pixels corresponding to 6.9 μm (fig. S3, A to C). The background fluorescence per pixel along the x axis was taken on the first pixel row at the top of the box and was subtracted to each box pixel. We then determined the intensity of the lipid, $i_{\mathrm{lip}}(x)$, and the intensity of actin, $i_{\mathrm{act}}(x)$, as the total fluorescence intensity along the vertical y axis (fig. S3B). The actin (resp. lipid) fluorescence was then defined as the average of the intensity along the variable x, $\langle i_{\mathrm{act}}(x)\rangle_x$ [resp. $\langle i_{\mathrm{lip}}(x)\rangle_x$]. The actin fluorescence per lipid fluorescence was determined as the ratio $\langle i_{\mathrm{act}}(x)\rangle_x/\langle i_{\mathrm{lip}}(x)\rangle_x$. Local intensities of actin or lipid [$I_{\mathrm{act}}(X)$ and $I_{\mathrm{lip}}(X)$, respectively] were sliding averaged as defined in fig. S3C.

The membrane tube radius was proportional to the number of fluorescently labeled lipids as described in (*45*) and shown in fig. S3D. To quantify heterogeneities along a membrane tube, after elongation, we define relative variation of radii along a tube, compared to the initial radius, as the relative variation of lipid fluorescence, compared to the initial lipid fluorescence: $\delta r/r_0 = \delta I_{\mathrm{lip}}/I_{\mathrm{lip},0} = (I^{\mathrm{m}}_{\mathrm{lip}} - I^{\mathrm{M}}_{\mathrm{lip}})/i_{\mathrm{lip},0}$, where the superscripts m and M respectively refer to the region where actin intensity is minimal (resp. maximal). When the lipid tube is homogeneous, δI_{lip} is not only centered around zero but can also have negative values due to our definition of m and M from the actin signal (fig. S3, A to C).

Characteristic relaxation and retraction times

At the end of elongation, force relaxation was fitted by a first-order decreasing exponential: $F(t) = A\ \exp(-t/\tau_{\mathrm{rel}}) + F_{\mathrm{fin}}$, where F_{fin} is the final value of the force. The maximal force after elongation is given by $F_{\mathrm{max}} = A + F_{\mathrm{fin}}$.

During retraction after the laser was turned off, we determined the tube length ℓ over time t by manual tracking using ImageJ. The characteristic retraction time τ_{ret} was determined by the fit $L(t) = a\ \exp(-t/\tau_{\mathrm{ret}}) + L_{\mathrm{fin}}$. We defined that there were partial retraction if L_{fin} were higher than 2 μm.

Statistical analysis

Results are represented as mean ± SEM. Graphs show the mean ± SD. All statistical analyses are performed using MedCalc software. A t test was used to determine the statistical significance, and P values are indicated (n.s., nonsignificant; $^{*}P < 0.05$, $^{**}P < 0.01$, and $^{***}P < 0.001$).

SUPPLEMENTARY MATERIALS

Supplementary material for this article is available at http://advances.sciencemag.org/cgi/content/full/6/17/eaaz3050/DC1

View/request a protocol for this paper from *Bio-protocol*.

REFERENCES AND NOTES

1. G. Egea, F. Lázaro-Diéguez, M. Vilella, Actin dynamics at the Golgi complex in mammalian cells. *Curr. Opin. Cell Biol.* **18**, 168–178 (2006).
2. C. A. Day, N. W. Baetz, C. A. Copeland, L. J. Kraft, B. Han, A. Tiwari, K. R. Drake, H. de Luca, D. J. F. Chinnapen, M. W. Davidson, R. K. Holmes, M. G. Jobling, T. A. Schroer, W. I. Lencer, A. K. Kenworthy, Microtubule motors power plasma membrane tubulation in clathrin-independent endocytosis. *Traffic* **16**, 572–590 (2015).
3. A. Roux, The physics of membrane tubes: soft templates for studying cellular membranes. *Soft Matter* **9**, 6726–6736 (2013).
4. P. S. Gurel, A. L. Hatch, H. N. Higgs, Connecting the cytoskeleton to the endoplasmic reticulum and Golgi. *Curr. Biol.* **24**, R660–R672 (2014).
5. J. Schöneberg, M. R. Pavlin, S. Yan, M. Righini, I.-H. Lee, L.-A. Carlson, A. H. Bahrami, D. H. Goldman, X. Ren, G. Hummer, C. Bustamante, J. H. Hurley, ATP-dependent force generation and membrane scission by ESCRT-III and Vps4. *Science* **362**, 1423–1428 (2018).
6. M. Kaksonen, C. P. Toret, D. G. Drubin, Harnessing actin dynamics for clathrin-mediated endocytosis. *Nat. Rev. Mol. Cell Biol.* **7**, 404–414 (2006).
7. S. Miserey-Lenkei, G. Chalancon, S. Bardin, E. Formstecher, B. Goud, A. Echard, Rab and actomyosin-dependent fission of transport vesicles at the Golgi complex. *Nat. Cell Biol.* **12**, 645–654 (2010).
8. E. Helfer, S. Harlepp, L. Bourdieu, J. Robert, F. C. MacKintosh, D. Chatenay, Viscoelastic properties of actin-coated membranes. *Phys. Rev. E* **63**, 021904 (2001).
9. I. Derényi, F. Jülicher, J. Prost, Formation and interaction of membrane tubes. *Phys. Rev. Lett.* **88**, 238101 (2002).
10. K. G. Campellone, N. J. Webb, E. A. Znameroski, M. D. Welch, WHAMM is an Arp2/3 complex activator that binds microtubules and functions in ER to golgi transport. *Cell* **134**, 148–161 (2008).
11. A. Capmany, A. Yoshimura, R. Kerdous, V. Caorsi, A. Lescure, E. D. Nery, E. Coudrier, B. Goud, K. Schauer, MYO1C stabilizes actin and facilitates the arrival of transport carriers at the Golgi complex. *J. Cell Sci.* **132**, jcs225029 (2019).
12. C. Leduc, O. Campàs, K. B. Zeldovich, A. Roux, P. Jolimaitre, L. Bourel-Bonnet, B. Goud, J. F. Joanny, P. Bassereau, J. Prost, Cooperative extraction of membrane nanotubes by molecular motors. *Proc. Natl. Acad. Sci. U.S.A.* **101**, 17096–17101 (2004).
13. C. Simon, R. Kusters, V. Caorsi, A. Allard, M. Abou-Ghali, J. Manzi, A. di Cicco, D. Lévy, M. Lenz, J. F. Joanny, C. Campillo, J. Plastino, P. Sens, C. Sykes, Actin dynamics drive cell-like membrane deformation. *Nat. Phys.* **15**, 602–609 (2019).
14. V. Noireaux, R. M. Golsteyn, E. Friederich, J. Prost, C. Antony, D. Louvard, C. Sykes, Growing an actin gel on spherical surfaces. *Biophys. J.* **78**, 1643–1654 (2000).
15. J. Plastino, C. Sykes, The actin slingshot. *Curr. Opin. Cell Biol.* **17**, 62–66 (2005).
16. O. Rossier, D. Cuvelier, N. Borghi, P. H. Puech, I. Derényi, A. Buguin, P. Nassoy, F. Brochard-Wyart, Giant vesicles under flows: Extrusion and retraction of tubes. *Langmuir* **19**, 575–584 (2003).
17. Y. Marcy, J. Prost, M.-F. Carlier, C. Sykes, Forces generated during actin-based propulsion: A direct measurement by micromanipulation. *Proc. Natl. Acad. Sci. U.S.A.* **101**, 5992–5997 (2004).
18. S. Plimpton, Fast parallel algorithms for short-range molecular dynamics. *J. Comp. Phys.* **117**, 1–19 (1995).
19. D. Feng, J. Notbohm, A. Benjamin, S. He, M. Wang, L.-H. Ang, M. Bantawa, M. Bouzid, E. del Gado, R. Krishnan, M. R. Pollak, Disease-causing mutation in α-actinin-4 promotes podocyte detachment through maladaptation to periodic stretch. *Proc. Natl. Acad. Sci. U.S.A.* **115**, 1517–1522 (2018).
20. M. Bouzid, E. Del Gado, Network topology in soft gels: Hardening and softening materials. *Langmuir* **34**, 773–781 (2017).
21. J. Irving, J. Kirkwood, The statistical mechanical theory of transport processes. IV. The equations of hydrodynamics. *J. Chem. Phys.* **18**, 817–829 (1950).
22. A. Thompson, S. Plimpton, W. Mattson, General formulation of pressure and stress tensor for arbitrary many-body interaction potentials under periodic boundary conditions. *J. Chem. Phys.* **131**, 154107 (2009).
23. F. Gittes, B. Mickey, J. Nettleton, J. Howard, Flexural rigidity of microtubules and actin filaments measured from thermal fluctuations in shape. *J. Cell Biol.* **120**, 923–934 (1993).
24. H. Isambert, P. Venier, A. C. Maggs, A. Fattoum, R. Kassab, D. Pantaloni, M. F. Carlier, Flexibility of actin filaments derived from thermal fluctuations. Effect of bound nucleotide, phalloidin, and muscle regulatory proteins. *J. Biol. Chem.* **270**, 11437–11444 (1995).
25. B. R. McCullough, L. Blanchoin, J.-L. Martiel, E. M. De la Cruz, Cofilin increases the bending flexibility of actin filaments: Implications for severing and cell mechanics. *J. Mol. Biol.* **381**, 550–558 (2008).
26. A. Kawska, K. Carvalho, J. Manzi, R. Boujemaa-Paterski, L. Blanchoin, J.-L. Martiel, C. Sykes, How actin network dynamics control the onset of actin-based motility. *Proc. Natl. Acad. Sci. U.S.A.* **109**, 14440–14445 (2012).
27. W. Helfrich, Elastic properties of lipid bilayers: Theory and possible experiments. *Z. Naturforsch. C* **28**, 693–703 (1973).
28. S. Dar, S. C. Kamerkar, T. J. Pucadyil, Use of the supported membrane tube assay system for real-time analysis of membrane fission reactions. *Nat. Protoc.* **12**, 390–400 (2017).
29. C. Campillo, P. Sens, D. Köster, L. L. Pontani, D. Lévy, P. Bassereau, P. Nassoy, C. Sykes, Unexpected membrane dynamics unveiled by membrane nanotube extrusion. *Biophys. J.* **104**, 1248–1256 (2013).
30. K. Guevorkian, J. Manzi, L. L. Pontani, F. Brochard-Wyart, C. Sykes, Mechanics of biomimetic liposomes encapsulating an actin shell. *Biophys. J.* **109**, 2471–2479 (2015).

31. P. Cicuta, S. L. Keller, S. L. Veatch, Diffusion of liquid domains in lipid bilayer membranes. *J. Phys. Chem. B* **111**, 3328–3331 (2007).
32. Y. A. Domanov, S. Aimon, G. E. S. Toombes, M. Renner, F. Quemeneur, A. Triller, M. S. Turner, P. Bassereau, Mobility in geometrically confined membranes. *Proc. Natl. Acad. Sci. U.S.A.* **108**, 12605–12610 (2011).
33. A. P. Liu, D. L. Richmond, L. Maibaum, S. Pronk, P. L. Geissler, D. A. Fletcher, Membrane-induced bundling of actin filaments. *Nat. Phys.* **4**, 789–793 (2008).
34. K. Carvalho, J. Lemière, F. Faqir, J. Manzi, L. Blanchoin, J. Plastino, T. Betz, C. Sykes, Actin polymerization or myosin contraction: Two ways to build up cortical tension for symmetry breaking. *Philos. Trans. R. Soc. B Biol. Sci.* **368**, 20130005 (2013).
35. K. Dürre, F. C. Keber, P. Bleicher, F. Brauns, C. J. Cyron, J. Faix, A. R. Bausch, Capping protein-controlled actin polymerization shapes lipid membranes. *Nat. Commun.* **9**, 1630 (2018).
36. U. Jelerčič, N. S. Gov, Pearling instability of membrane tubes driven by curved proteins and actin polymerization. *Phys. Biol.* **12**, 066022 (2015).
37. B. J. Peter, H. M. Kent, I. G. Mills, Y. Vallis, P. J. G. Butler, P. R. Evans, H. T. McMahon, BAR domains as sensors of membrane curvature: The amphiphysin BAR structure. *Science* **303**, 495–499 (2004).
38. A. Roux, G. Koster, M. Lenz, B. Sorre, J.-B. Manneville, P. Nassoy, P. Bassereau, Membrane curvature controls dynamin polymerization. *Proc. Natl. Acad. Sci. U.S.A.* **107**, 4141–4146 (2010).
39. M. Simunovic, J.-B. Manneville, H.-F. Renard, E. Evergren, K. Raghunathan, D. Bhatia, A. K. Kenworthy, G. A. Voth, J. Prost, H. T. Mc Mahon, L. Johannes, P. Bassereau, A. Callan-Jones, Friction mediates scission of tubular membranes scaffolded by BAR proteins. *Cell* **170**, 172–184.e11 (2017).
40. M. I. Angelova, D. S. Dimitrov, Liposome electroformation. *Faraday Discuss. Chem. Soc.* **81**, 303–311 (1986).
41. S. Palmgren, P. J. Ojala, M. A. Wear, J. A. Cooper, P. Lappalainen, Interactions with PIP_2, ADP-actin monomers, and capping protein regulate the activity and localization of yeast twinfilin. *J. Cell Biol.* **155**, 251–260 (2001).
42. S. Havrylenko, P. Noguera, M. Abou-Ghali, J. Manzi, F. Faqir, A. Lamora, C. Guérin, L. Blanchoin, J. Plastino, WAVE binds Ena/VASP for enhanced Arp2/3 complex–based actin assembly. *Mol. Biol. Cell* **26**, 55–65 (2015).
43. F. Valentino, P. Sens, J. Lemière, A. Allard, T. Betz, C. Campillo, C. Sykes, Fluctuations of a membrane nanotube revealed by high-resolution force measurements. *Soft Matter* **12**, 9429–9435 (2016).
44. F. Gittes, C. F. Schmidt, Interference model for back-focal-plane displacement detection in optical tweezers. *Opt. Lett.* **23**, 7–9 (1998).
45. S. Aimon, A. Callan-Jones, A. Berthaud, M. Pinot, G. E. S. Toombes, P. Bassereau, Membrane shape modulates transmembrane protein distribution. *Dev. Cell* **28**, 212–218 (2014).

Acknowledgments: C.Sy. acknowledges A. Echard and B. Goud for initiating initial discussions about the possible role of actin on membrane tubule stability and scission. We acknowledge the Imaging Centre at BDD-Institut Curie for providing the microscope with a FRAP module. **Funding:** This work was supported by the French Agence Nationale pour la Recherche (ANR) grants ANR 09BLAN0283, ANR 12BSV5001401, ANR 15 CE13000403, and ANR 18 CE13000701; by the Fondation pour la Recherche Médicale grant DEQ20120323737, and FDT201904007966; the ERC Starting Grant 677532; and the ERC COnsolidator Grant 771201; by the ANR-PSL-LabEx CelTisPhyBio. **Author contributions:** A.A. performed experiments and analyzed the data. M.B. performed the simulations. M.L. and F.B.-W. developed the theoretical models. T.B., C.Si., M.A.-G., J.L., F.V., K.G., J.P., and C.C. contributed to the experimental data. J.M. purified the proteins. T.B., C.C., and C.Sy. designed the research. All authors contributed to the writing of the paper. **Competing interests:** The authors declare that they have no competing interests. **Data and materials availability statement:** All data needed to evaluate the conclusions in the paper are present in the paper and/or the Supplementary Materials. Additional data related to this paper may be requested from the authors.

Submitted 28 August 2019
Accepted 21 January 2020
Published 22 April 2020
10.1126/sciadv.aaz3050

Citation: A. Allard, M. Bouzid, T. Betz, C. Simon, M. Abou-Ghali, J. Lemière, F. Valentino, J. Manzi, F. Brochard-Wyart, K. Guevorkian, J. Plastino, M. Lenz, C. Campillo, C. Sykes, Actin modulates shape and mechanics of tubular membranes. *Sci. Adv.* **6**, eaaz3050 (2020).